

Local primordial non-Gaussianity from the large-scale clustering of photometric DESI luminous red galaxies

Mehdi Rezaie¹, Ashley J. Ross², Hee-Jong Seo³, Hui Kong³, Edmond Chaussidon⁴, Anna Porredon³, Lado Samushia¹, Rongpu Zhou⁵, Alex Krolewski^{6,7,8}, Arnaud de Mattia⁴, Jose Bermejo⁷, Florian Beutler⁹, Christophe Yèche⁴, Nathalie Palanque-Delabrouille^{4,5}, Klaus Honscheid^{2,10}, and DESI Builders

¹*Department of Physics, Kansas State University, 116 Cardwell Hall, Manhattan, KS 66506, USA*

²*Department of Physics and Astronomy, Ohio University, Athens, OH 45701, USA*

³*Center for Cosmology and AstroParticle Physics, The Ohio State University, 191 West Woodruff Avenue, Columbus, OH 43210, USA*

⁴*IRFU, CEA, Université Paris-Saclay, F-91191 Gif-sur-Yvette, France*

⁵*Lawrence Berkeley National Laboratory, 1 Cyclotron Road, Berkeley, CA 94720, USA*

⁶*Department of Physics and Astronomy, University of Waterloo, 200 University Ave W, Waterloo, ON N2L 3G1, Canada*

⁷*Perimeter Institute for Theoretical Physics, 31 Caroline St. North, Waterloo, ON N2L 2Y5, Canada*

⁸*Waterloo Centre for Astrophysics, University of Waterloo, 200 University Ave W, Waterloo, ON N2L 3G1, Canada*

⁹*Institute for Astronomy, University of Edinburgh, Royal Observatory, Blackford Hill, Edinburgh EH9 3HJ, UK*

¹⁰*Department of Physics, The Ohio State University, 191 West Woodruff Avenue, Columbus, OH 43210, USA*

Accepted XXX. Received YYY; in original form ZZZ

ABSTRACT

This paper uses the large-scale clustering of luminous red galaxies selected from the Dark Energy Spectroscopic Instrument Legacy Imaging Surveys Data Release 9 to constrain the local primordial non-Gaussianity (PNG) parameter f_{NL} . We thoroughly investigate the impact of various photometric systematic effects, such as those caused by Galactic extinction, local stellar density, varying survey depth, and seeing using spherical harmonics cross power spectrum and mean galaxy density. Lognormal density fields are simulated with and without PNG, and utilized to construct covariance matrices, evaluate the robustness of our pipeline, assess whether spurious fluctuations are properly mitigated, and calibrate our cleaning methods. Using harmonic modes from $\ell = 2$ to 300, we find $36.07(25.03) < f_{\text{NL}} < 61.44(75.64)$ with a conservative cleaning approach and $13.09(-15.95) < f_{\text{NL}} < 69.14(91.84)$ with an extreme treatment of imaging systematics, both at 68%(95%) confidence. We find that calibration issues in the South Galactic Cap and local stellar density in the North Galactic Cap indicate some remaining systematic error, which induce significant biases in f_{NL} constraints. While our constraints are consistent with zero PNG at 95% confidence for the extreme approach, we show that the characterization of stellar contamination and calibration issues are crucial to derive unbiased constraints on f_{NL} in the era of DESI and LSST cosmology.

Key words: cosmology: inflation - large-scale structure of the Universe

1 INTRODUCTION

Current observations of the cosmic microwave background (CMB), large-scale structure (LSS), and supernovae (SN) Hubble diagrams are explained to a great degree by a cosmological model that consists of dark energy, dark matter, and ordinary luminous matter, which has gone through a phase of rapid expansion, known as *inflation*, at its early stages (see, e.g., Weinberg et al. 2013). The paradigm of inflation elegantly addresses fundamental issues, such as the isotropy, flatness, and homogeneity of the Universe as well as the absence of magnetic monopole (see, e.g., Weinberg 2008).

At the end of inflation, the Universe went through a reheating process, and primordial fluctuations generated to seed the subsequent growth of structure (Kofman et al. 1994; Bassett et al. 2006; Lyth & Liddle 2009). Even though the reality of an inflationary era is almost certain from observations, the details of the inflation field and its underlying mechanism are vastly unknown, and statistical properties of primordial fluctuations remain an interesting question in modern observational cosmology. Early analyses of cosmological datasets have suggested that initial conditions of the Universe are consistent with Gaussian fluctuations (Guth & Kaiser 2005); however, some classes of inflationary models predict some levels of

non-Gaussianities in the primordial gravitational field. In its simplest form, primordial non-Gaussianity (PNG) depends on the local value of the gravitational potential ϕ , and it is parameterized by a nonlinear coupling constant f_{NL} (Komatsu & Spergel 2001),

$$\Phi = \phi + f_{\text{NL}}[\phi^2 - \langle \phi^2 \rangle]. \quad (1)$$

Standard slow-roll inflation predicts f_{NL} to be of order 10^{-2} , while multi-field inflationary theories anticipate considerably higher values than unity (see, e.g., de Putter et al. 2017). Therefore, deriving robust constraints on f_{NL} are considered the first stepping stone toward better understanding the physics of the early Universe. PNG alters the local number density of galaxies by coupling the long and small wavelength modes of dark matter gravitational field, and as a result, it induces a scale-dependent shift in halo bias (see, e.g., Dalal et al. 2008; Slosar et al. 2008),

$$\Delta b \sim f_{\text{NL}} \frac{(b-p)}{k^2}, \quad (2)$$

where p determines the response of the tracer to the halo gravitational field. If only mass determines how galaxies occupy a halo, $p = 1$, which is often referred to as the universality of halo occupation function. However, numerical simulations have shown halo occupation distribution of tracers that resulted from recent mergers could depend on more properties besides mass, and thus $p = 1.6$ (Slosar et al. 2008). Because of the dependence of Δb on k^{-2} , local primordial non-Gaussianity leaves its signature on small wavenumbers (or large scales) in the two-point clustering of galaxies and quasars.

The current tightest bound on f_{NL} comes from the three-point clustering analysis of the CMB temperature anisotropies by the Planck satellite, $f_{\text{NL}} = 0.9 \pm 5.0$ (Akrami et al. 2019). Upcoming generations of CMB experiments will improve this constraint, but since cosmic variance limits CMB, CMB data alone cannot further enhance our understanding of f_{NL} enough to break the degeneracy amongst inflationary models (see, e.g., Ade et al. 2019). However, combining CMB with LSS data could cancel cosmic variance, partially even if not completely, and enhance these limits to a precision level required to differentiate between various inflationary models (see, e.g., Schmittfull & Seljak 2018). Constraining f_{NL} with the three-point clustering of LSS is also hindered by the late-time non-linear effects raised due to structure growth (Baldauf et al. 2011b,a), and this limitation establishes the scale-dependent bias effect as the smoking gun for constraining local PNG with LSS. UV Luminosity Function probes galaxy abundances and structure formation on small scales (e.g., $k \sim 2 \text{ Mpc}^{-1}$), which are otherwise impossible to explore with CMB and LSS, and provides a new approach for constraining f_{NL} . With this technique, Sabti et al. (2021) uses the Hubble Space Telescope catalogs (Bouwens et al. 2015) to find a 2σ bound of $-166 < f_{\text{NL}} < 497$, and predicts upcoming surveys such as the James Webb Space Telescope and the Nancy Grace Roman Space Telescope to yield up to four times improvements.

Measuring f_{NL} with the scale-dependent bias effect is nonetheless exceptionally challenging due to various systematic effects which spur excess clustering signal on large scales sensitive to f_{NL} . These systematics are broadly classified into theoretical and observational. Survey geometry is a major source of systematic error, which couples clustering power at different angular modes (Beutler et al. 2014; Wilson et al. 2017). Relativistic effects also generate identical scale-dependent signatures on large scales, which hinder measuring f_{NL} with the scale-dependent bias effect (Wang et al. 2020). Similarly, matter density fluctuations with wavelengths larger than survey volume, known as super-sample modes, modulate power spectrum of galaxies (Castorina & Moradinezhad Dizgah

2020). Integral constraint is raised because the mean galaxy density for constructing the density contrast field is estimated from data directly rather than being known a priori. Integral constraint pushes clustering power on modes near survey size to zero (Peacock & Nicholson 1991; De Mattia & Ruhlmann-Kleider 2019). Neglecting any of these effects in modeling power spectrum leads to biased f_{NL} constraints (Riquelme et al. 2022, see, e.g.,). On the other hand, observational systematics are driven predominantly by either varying imaging properties across the sky (Ross et al. 2011) or calibration issues that cause spurious fluctuations in the target density field (Huterer et al. 2013). This type of systematic error is much more challenging to model and mitigate, and it has hampered previous studies of local PNG with the scale-dependent bias effect and clustering of galaxies and quasars (see, e.g., Ho et al. 2015). For instance, Pullen & Hirata (2013) found that the level of systematic contamination in the quasar sample of Sloan Digital Sky Survey DR6 does not allow a robust f_{NL} measurement. These imaging systematic issues are expected to be severe for wide-area galaxy surveys that observe the night sky closer to the Galactic plane and attempt to loosen the selection criteria to incorporate fainter targets (see, e.g., Kitanidis et al. 2020). Besides canceling cosmic variance, cross-correlating different tracers is another technique to alleviate the impact of imaging systematics, as each tracer might respond differently to a source of systematics. Giannantonio et al. (2014) presents improved f_{NL} constraints using the integrated Sachs-Wolfe effect.

The Dark Energy Spectroscopic Instrument (DESI) uses robots to collect 5000 spectra in parallel, and is designed to deliver unparalleled volume of spectroscopic data that will enable analyses to deepen our understanding of the energy contents of the Universe, specifically, the equation of state for Dark Energy. Assuming imaging systematics are under control and with the volume probed, DESI along with other upcoming surveys, such as Rubin Observatory and SphereX, are expected to yield unprecedented constraints on f_{NL} (see, e.g., Heinrich & Doré 2022). DESI preselects its targets from its dedicated imaging surveys, known as the DESI Legacy Imaging Surveys, which are collected from observation conducted between 2014 and 2019 from three ground-based telescopes based in Chile and the US.

The characterization of potential sources for systematic error in DESI imaging data is of paramount importance to DESI success, since these effects from imaging catalogs could potentially be inherited into spectroscopic catalogs and thus negatively influence the science goals with DESI data. DESI targets galaxies and quasars to construct a 3D map of LSS up to redshifts around 4. The effects of observational systematics in DESI targets have been studied in great detail (see, e.g., Kitanidis et al. 2020; Zhou et al. 2021; Chausidon et al. 2022). Improving techniques to characterize systematic error in these samples is crucial for the science beyond dark energy, such as constraining f_{NL} . Some of the current methods seek to mitigate systematic effects by either cross-correlating target density and imaging maps (mode deprojection) or solving a least-square optimization to estimate the contribution from each imaging property to target density field (template-based regression), ultimately to regress out the modes affected by imaging properties from the target density. These methods have their limitations and strengths. For instance, mode deprojection yields an unbiased clustering but can be employed for angular clustering only, and its involved matrix algebra could turn out time-consuming for large survey sizes. Template-based regression is computationally inexpensive, but it returns biased clustering by removing some of clustering signal, depending on the number of templates and the flexibility of regres-

sion model. Specifically related to the template-based regression method, there is little effort to calibrate and characterize the amount of clustering power, which is removed during the cleaning process. For studies like BAO and RSD, these effects are demonstrated to be negligible (Merz et al. 2021); however, these effects introduce biases in f_{NL} constraints (Mueller et al. 2022) as they are prominent on large scales (Rezaie et al. 2021).

This paper presents an exquisite study of imaging systematic error and characterization of mitigation biases for constraining f_{NL} with the DESI imaging data. We address the sample quality and measure the significance of residual systematic error with angular cross power spectrum (between galaxy density and imaging properties) and galaxy mean density contrast statistics. In this paper, the robustness of our results is validated against various sources of systematic error, such as calibration and Milky Way extinction. We utilize early spectroscopic data from the DESI Survey Validation to determine the redshift distribution of tracers used for our analysis. We cross-correlate the galaxy density field with the templates of imaging properties to evaluate the effectiveness of different treatment methods and to characterize the significance of residual systematic error. To assess the sensitivity of f_{NL} signal to cleaning methods, we apply various linear and nonlinear approaches with different combinations of template maps for imaging properties. This paper is structured as follows. Section 2 describes the DESI imaging galaxy sample and simulations with and without PNG and imaging systematic effects, and Section 3 outlines the theory framework for modeling angular power spectrum and analysis techniques to account for various observational and theoretical systematic error. Finally, we present f_{NL} constraints in Section 4, and conclude with a comparison to previous f_{NL} studies in Section 5.

2 DATA

Luminous red galaxies (LRGs) are massive galaxies that occupy massive halos, lack active star formation, and are one of the highly biased tracers of large scale structure. Redshifts of LRGs are easily determined from a break around 4000 Å in their spectra. LRGs are widely targeted in previous galaxy redshift surveys (see, e.g., Eisenstein et al. 2001; Prakash et al. 2016), and their clustering and redshift properties are well studied (see, e.g., Alam et al. 2021). DESI is designed to collect spectra of millions of LRGs covering the redshift range of $0.4 < z < 1.0$ over the span of its five-year mission. Targets for DESI spectroscopy are pre-selected from three ground-based imaging surveys that probed the night sky in the optical bands between 2014 and 2019: the Mayall z-band Legacy Survey using the Mayall telescope at Kitt Peak (Dey et al. 2018), the Beijing–Arizona Sky Survey using the Bok telescope at Kitt Peak (Zou et al. 2017), and the Dark Energy Camera Legacy Survey on the Blanco 4m telescope (DECaLS Flaugher et al. 2015). Additionally, the DECaLS program integrates observations conducted from the same instrument under the Dark Energy Survey (Abbott et al. 2016), which constitute about 1130 deg² of their southern sky footprint. The BASS+MzLS footprint is distinguished from the DECaLS NGC by applying DEC > 32.375 degrees, although there is an overlap between the two region for calibration (Dey et al. 2018).

2.1 DESI Imaging DR9 LRGs

We work with the photometric LRGs selected from the DESI Imaging Surveys Data Release 9 (DR9; Dey et al. 2018) using the selection and cuts designed for the DESI 1% survey (CITE), described

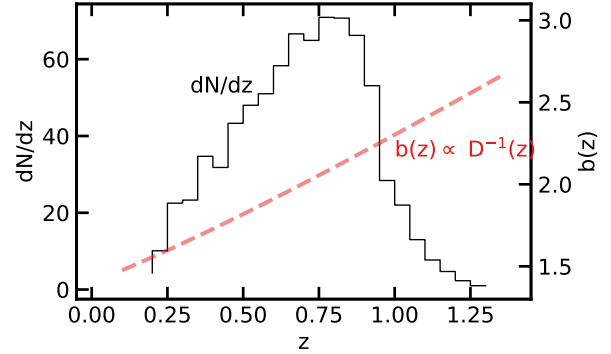


Figure 1. Redshift distribution (solid) and bias evolution (dashed) of DESI LRGs (Zhou et al. 2021, 2022). The LRG redshift distribution is deducted from early spectroscopy by DESI and the LRG bias model assumes a constant clustering amplitude.

as SV3 selection in more detail in Zhou et al. (2022). The color-magnitude selection cuts are defined in the g , r , z bands in the optical and W1 band in the infrared frequencies, and summarized in Tab. 1. The implementation of these selection cuts in the DESI data processing pipeline is described in Myers et al. (2022). Fig. 1 shows the redshift distribution of our LRG sample (solid black) which is inferred from the spectroscopic DESI Survey Validation data (CITE), and the evolution of halo bias for our LRG sample (dashed red) adapted from Zhou et al. (2021). The bias model is consistent with the assumption of a constant clustering amplitude.

DESI-like LRGs are selected brighter than the survey depth limits; therefore, the LRG density field is nearly homogenous unlike other DESI tracers. To further reduce stellar contamination, the LRG sample is masked rigorously for foreground bright stars, galaxies, and clusters of galaxies¹. Then, the sample is binned into HEALPIX (Gorski et al. 2005) at NSIDE = 256 to construct the density map with an average surface density of 800 deg⁻² with sky coverage around 14,000 square degrees. The density map is corrected for pixel incompleteness and masked areas in the density field of LRGs using a catalog of random points, hereafter referred to as randoms, uniformly scattered over the footprint with the same cuts and masks applied to the DR9 LRGs. Fig. 2 (top) shows observed density field of the DR9 LRGs in deg⁻² before accounting for any imaging systematic effects, which demonstrates large-scale spurious fluctuations. Specifically, the SGC footprint indicates some systematic under-density while there are some systematic overdensity near the boundaries in the NGC. There are some disconnected islands, hereafter referred to as *spurious islands*, in the DECaLS North region at Declination below −11, which are removed from the main analysis to minimize potential calibration issues. Additionally, some parts of the DECaLS South footprint with Declination below −30 are removed from the sample, since similar calibration issues might tamper with our analysis. We present how these data cuts influence our f_{NL} constraints in Section 4.

We study the impact of imaging properties as potential sources of systematic error, mapped into HEALPIX at the same NSIDE. Similar to Zhou et al. (2022), the properties studied in this work are local stellar density constructed from point-like sources with a g -band magnitude in the range $12 \leq g < 17$ from Gaia Data Release 2 (see, Gaia Collaboration et al. 2018; Myers et al. 2022); Galactic

¹ See the maskbits at <https://www.legacysurvey.org/dr9/bitmasks/>

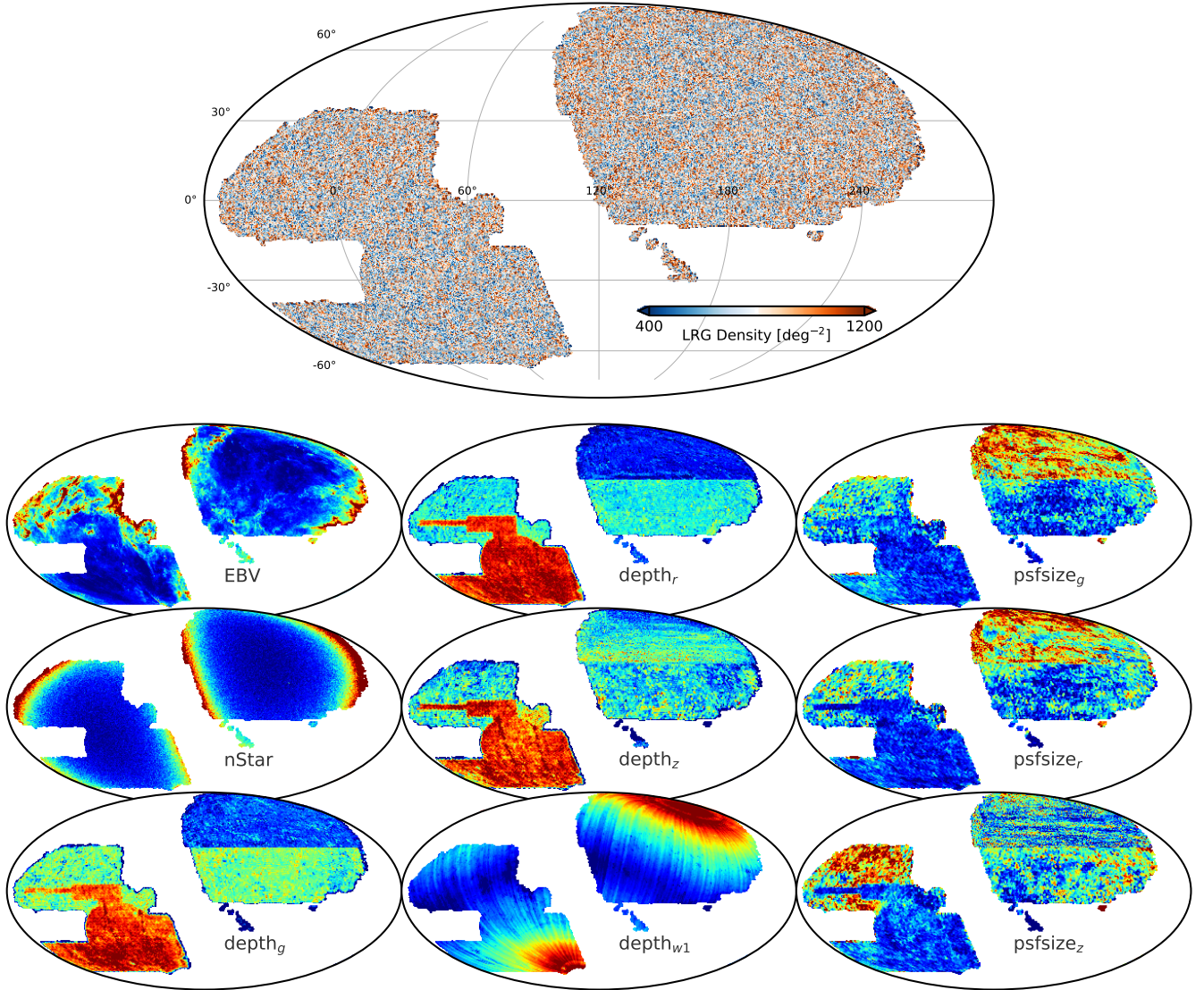


Figure 2. DESI Imaging Legacy Survey Data Release 9 Luminous Red Galaxies and imaging properties (Dey et al. 2018). Top: Observed target density field in deg^{-2} . Spurious disconnected islands from the DECaLS North footprint at Declination below -11 and parts of the DECaLS South with Declination below -30 are dropped from the DR9 sample due to potential calibration issues. Bottom: Mollweide projections of DR9 catalog imaging properties (depth and psfsize/seeing) and MW foregrounds (extinction and local stellar density) in celestial coordinates.

extinction $E[B-V]$ from Schlegel et al. (1998); and other imaging properties include survey depth (galaxy depth in the g, r, and z bands and PSF depth in W1) and seeing in the g, r, and z bands. These maps are produced by making the histograms of randoms (painted with imaging properties) in HEALPix and averaging over randoms in each pixel. Fig. 2 (bottom) illustrates the imaging templates investigated for potential sources of systematic error, each of which reflect their characteristic large-scale spurious fluctuations. For instance, the underdensity with the SGC can be visually correlated with the depth maps, while the overdensity in the NGC can be associated visually with the extinction map.

Fig. 3 shows the Pearson correlation coefficient between the DR9 LRG density and DESI imaging properties for the three imaging surveys (DECaLS North, DECaLS South, and BASS+MzLS) in the top panel and the correlation matrix among the imaging properties themselves for the full DESI survey in the bottom panel.

There is a strong correlation between the LRG density and depth maps, and then the second correlated property seems to be Galactic foregrounds. There is a little correlation between the LRG density and the W1 depth and psfsize properties. We find that there is a large correlation among the imaging properties themselves, especially between the local stellar density and Milky Way extinction; also, the r-band and g-band properties are more correlated with each other than with the z-band. We follow a template-based approach to derive a set of weights to apply to the LRG density in order to account for spurious fluctuations. We regress out the DR9 density map against a set of imaging maps, referred to as imaging templates. Because of the inner-correlation amongst the maps, a few subsets of maps are considered as well. These subsets are selected to minimize the correlations among the predictors while having maximum correlation with observed density map.

- Conservative I: Extinction, depth_z

Table 1. Selection criteria for the DESI-like LRG targets (Zhou et al. 2022). Magnitudes are corrected for MW extinction.

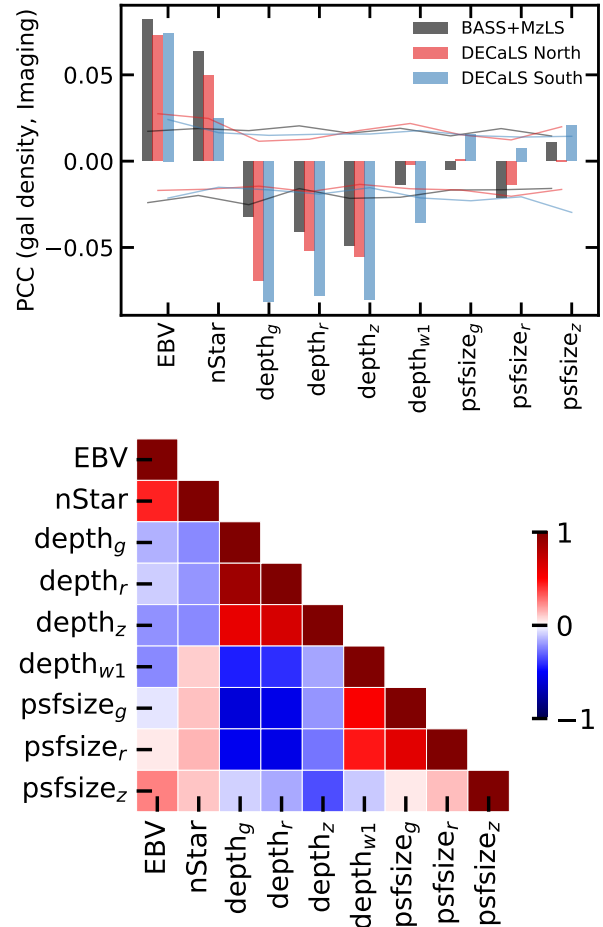
Footprint	Criterion	Description
DECaLS	$z_{\text{fiber}} < 21.7$	Faint limit
	$z - W1 > 0.8 \times (r - z) - 0.6$	Stellar rejection
	$[(g - r > 1.3) \text{ AND } ((g - r) > -1.55 * (r - W1) + 3.13)] \text{ OR } (r - W1 > 1.8)$	Remove low- z galaxies
	$[(r - W1 > (W1 - 17.26) * 1.8) \text{ AND } (r - W1 > W1 - 16.36)] \text{ OR } (r - W1 > 3.29)$	Luminosity cut
BASS+MzLS	$z_{\text{fiber}} < 21.71$	Faint limit
	$z - W1 > 0.8 \times (r - z) - 0.6$	Stellar rejection
	$[(g - r > 1.34) \text{ AND } ((g - r) > -1.55 * (r - W1) + 3.23)] \text{ OR } (r - W1 > 1.8)$	Remove low- z galaxies
	$[(r - W1 > (W1 - 17.24) * 1.83) \text{ AND } (r - W1 > W1 - 16.33)] \text{ OR } (r - W1 > 3.39)$	Luminosity cut

- Conservative II: Extinction, depth_z , psfsiz_r
- All Maps: Extinction, depth in grz and $W1$, psfsiz_r in grz

We also investigate whether including external maps for neutral hydrogen column density (CITE) and calibration (e.g., in the z band; CALIBZ) could shed light on remaining systematic effects.

Linear and nonlinear models (approximated using a neural network) are applied to assess the potential of nonlinear systematic error. Parameters of the models are fit by optimizing the negative Poisson log likelihood, $= \sum \lambda - \rho \log(\lambda)$, where the summation runs over pixels, ρ is the galaxy density, and λ is either a linear or nonlinear model for galaxy density given imaging properties \mathbf{x} as input, $\lambda(\mathbf{x}) = \log(1 + e^{f(\mathbf{x})})$. For finding the parameters of the linear model, we perform a Monte Carlo Markov Chain (MCMC) search using the EMCEE package (CITE) and for the nonlinear model we use the implementation from Rezaie et al. (2021); specifically, the nonlinear model is an ensemble of 20 neural network models. Each neural network is constructed with three hidden layers and 20 rectifier units on each layer. Rectifier is identity function for positive input and zero for negative, and it introduces nonlinearities in the neural network. For the linear model we use all data for computing the log of posterior during MCMC while for the nonlinear approach we use 60% of data for training, 20% for validation, and 20% for testing; this is to minimize the chance of over-fitting by the nonlinear model. By changing the permutation of training-testing splits, we test the nonlinear model on entire data. The training is performed for up to 70 training epochs using ADAM optimizer, which is a variant of gradient descent, and the learning rate is tuned on the validation set to dynamically varying between 0.001 and 0.1, to enable learning robust against local minima. The best model is then selected with the lowest prediction error when applied to the validation set. Finally, we apply the ensemble of 20 best fit models to the test set and average over the predictions to construct the predicted galaxy density maps, which is inverted and used as imaging systematic weights.

Upon the inspection of the predicted density maps, we find that while most of the large-scale spurious fluctuations are explained by just the extinction map and depth in the z band, adding the psfsiz_r in the r band results in finer structure in the predicted density map. Using all maps as input features for regression does not add much information. Comparing linear to nonlinear with the same input maps, we find that the nonlinear approach yields finer structure due to a higher flexibility. Overall, both models predict higher density near the boundaries where the surveys meet the high extinction regions of Milky Way. These regions are probably contaminated artifacts entering the selection either via the direct stellar contamination or the impact of extinction on colors.


Figure 3. Top: Pearson-r correlation coefficient between galaxy density and imaging properties in the three imaging regions. Solid curves represent the range of correlations observed in 100 randomly selected mock density realizations. Bottom: Pearson-r correlation matrix between imaging properties themselves for the full DESI footprint.

2.2 Synthetic lognormal density fields

Lognormal distributions are shown to be appropriate for describing matter density fluctuations on large scales (Coles & Jones 1991). Unlike N-body simulations, the generation of lognormal density fields is rather quick and enables a computationally economic approach to generate a large ensemble of synthetic realizations of galaxy density fields which mimic the redshift and angular distribution of real data. Mocks will enable the validation of analysis software from an end-to-end perspective, and mocks can be used to construct covariance matrices for error estimation and per-

form statistical tests for characterizing remaining systematic effects. FLASK (Full-sky Lognormal Astro-fields Simulation Kit; [Xavier et al. 2016](#)) is used to generate series of lognormal galaxy density fields with $f_{\text{NL}} = 0$ and 76.92 using a redshift dependent bias $b(z) = 1.43/D(z)$. 1000 realizations are generated for each f_{NL} . The fiducial cosmology to generate the mocks is based on a flat Λ CDM universe including one massive neutrino with $m_\nu = 0.06$ eV, and the rest of cosmological parameters are chosen within 68% of the Planck 2018 results ([Aghanim et al. 2020](#)),

$$h = 0.67, \Omega_M = 0.31, \sigma_8 = 0.8, \text{ and } n_s = 0.97.$$

We use the same fiducial cosmology for the analysis of DR9 sample. Our robustness tests indicate that these parameters are not degenerate with f_{NL} , and thus fixing them would not induce biases in f_{NL} constraints.

3 ANALYSIS TECHNIQUES

This section describes the estimator for measuring the angular power spectrum and the methodology for modeling it in the presence of PNG. We also demonstrate how we correct for the effects of survey geometry and integral constraint in the modeling. The statistical tools for measuring the remaining systematic error are also presented.

3.1 Measuring Power Spectrum

The quantity that carries cosmological information is galaxy density contrast, δ , which in pixel i is constructed as,

$$\hat{\delta}_i = \frac{\rho_i}{\bar{\rho}} - 1, \quad (3)$$

where ρ is the density of galaxies accounted for pixel area $f_{\text{pix},i}$, which is determined by uniformly distributed random galaxies over footprint, and $\bar{\rho}$ is the mean galaxy density directly estimated from the data,

$$\hat{\bar{\rho}} = \frac{\sum_i \rho_i f_{\text{pix},i}}{\sum_i f_{\text{pix},i}}. \quad (4)$$

By definition, Eqs. 3 and 4 ensure that the integral of the observed quantity over the footprint vanishes:

$$\sum_i \hat{\delta}_i f_{\text{pix},i} = 0, \quad (5)$$

and this constraint causes an effect commonly referred to as *integral constraint*, which needs to be accounted for in the model. To estimate power spectrum, the galaxy density contrast is expanded in terms of Legendre polynomials,

$$\hat{\delta}_i = \sum_{\ell=0}^{\ell_{\text{max}}} \sum_{m=-\ell}^{\ell} a_{\ell m} Y_{\ell m}(\theta_i, \phi_i), \quad (6)$$

where θ, ϕ represent the polar and azimuthal angular coordinates of pixel i center, respectively. The cutoff at $\ell = \ell_{\text{max}}$ assumes that modes with $\ell > \ell_{\text{max}}$ do not contribute significantly to signal power. The coefficients $a_{\ell m}$ are then obtained by integrating the density contrast field over the total number of non-empty pixels N_{pix} and using the orthogonality of Legendre polynomials:

$$\hat{a}_{\ell m} = \frac{4\pi}{N_{\text{pix}}} \sum_{i=1}^{N_{\text{pix}}} \hat{\delta}_i f_{\text{pix},i} Y_{\ell m}^*(\theta_i, \phi_i), \quad (7)$$

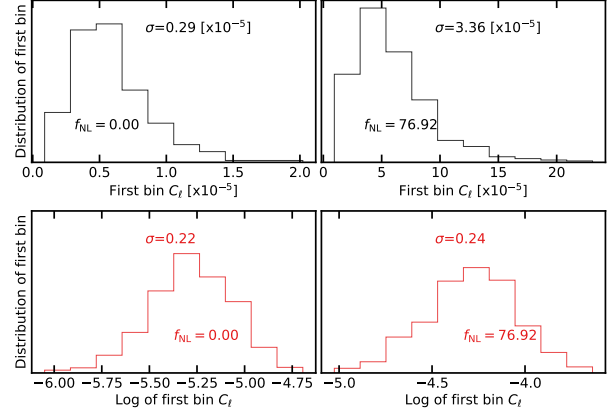


Figure 4. Distribution of the first bin power spectrum constructed from $f_{\text{NL}} = 0$ (left) and 76.92 (right) mocks. Differences in the standard deviations become less significant, and power spectrum measurements follow a more symmetric distribution after the log transformation.

where $*$ represents the complex conjugate. Then, the angular power spectrum estimator is defined as the variance of $\hat{a}_{\ell m}$ coefficients:

$$\hat{C}_\ell = \frac{1}{2\ell+1} \sum_{m=-\ell}^{\ell} \hat{a}_{\ell m} \hat{a}_{\ell m}^*. \quad (8)$$

In order to extract $\hat{a}_{\ell m}$ and compute the angular power spectrum, C_ℓ , the function ANAFast is called from HEALPIX ([Gorski et al. 2005](#)) with the third order iteration of the quadrature to increase the accuracy². Due to the survey geometry implicit in the summation over the non-empty pixels and explicit in $f_{\text{pix},i}$, our estimator does not return an unbiased estimate of power spectrum, as different harmonic modes are no longer independent. Therefore, we account for the same effect in the modeling of angular power spectrum. The survey geometry treatment is validated against synthetic datasets.

3.2 Modeling Power Spectrum

Angular power spectrum is a projection of 3D clustering along the line of sight over all possible wavenumbers k . With redshift space distortions included, the projected angular power spectrum of galaxies is related to the 3D linear power spectrum $P(k)$ and shotnoise N_{shot} by (see, e.g., [Padmanabhan et al. 2007](#)),

$$C_\ell = \frac{2}{\pi} \int_0^\infty \frac{dk}{k} k^3 P(k) |\Delta_\ell(k)|^2 + N_{\text{shot}}, \quad (9)$$

where shotnoise is assumed to scale-independent, and kernel $\Delta_\ell(k) = \Delta_\ell^g(k) + \Delta_\ell^{\text{RSD}}(k)$ determines how much each wavenumber k contributes to ℓ by integrating over all comoving distances r and accounting for cosmic growth,

$$\Delta_\ell^g(k) = \int \frac{dr}{r} r b(r) D(r) \frac{dN}{dr} j_\ell(kr), \quad (10)$$

$$\Delta_\ell^{\text{RSD}}(k) = - \int \frac{dr}{r} r f(r) D(r) \frac{dN}{dr} j_\ell''(kr), \quad (11)$$

where $D(r)$ is the normalized growth factor such that $D(0) = 1$, $f(r)$ is the growth rate, and dN/dr is the normalized redshift distribution of galaxies³ (see, Fig. 1). In the presence of local primordial

² We refer the reader to <https://healpix.sourceforge.io/pdf/subroutines.pdf>, p. 104-105.

³ $dN/dr = (dN/dz) * (dz/dr) \propto (dN/dz) * H(z)$

non-Gaussianity, $b(r)$ is the linear bias b (see, Fig. 1) plus the scale-dependent shift due to PNG (see, Eq. 2),

$$b(k, r) = b + \frac{2(b-p)f_{\text{NL}}\delta_c}{\alpha(k)}, \quad (12)$$

where $\alpha(k) \propto k^2$, $\delta_c = 1.686$ is the critical density above which gravitational collapse occurs (Fillmore & Goldreich 1984), and the parameter p determines the response of the tracer to halo's gravitational field, e.g., 1 for luminous red galaxies following universality and 1.6 for tracers that are results of recent mergers like quasars. In order to overcome rapid oscillations in spherical Bessel functions, FFTLog⁴ algorithm and its extension as implemented in Fang et al. (2020) are employed to evaluate the inner integrations over $d \ln r$.

For a galaxy survey that observes the sky partially, the measured power spectrum is convolved with the survey geometry. This means that the pseudo-power spectrum \hat{C}_ℓ obtained by the direct Spherical Harmonic Transforms of a partial sky map, differs from the full-sky angular spectrum C_ℓ . However, their ensemble average is related by a mixing matrix (Hivon et al. 2002),

$$\langle \hat{C}_\ell \rangle = \sum_{\ell'} M_{\ell\ell'} \langle C_{\ell'} \rangle, \quad (13)$$

where $M_{\ell\ell'}$ represents the mode-mode coupling from the partial sky coverage. This is known as the Window Function effect and a proper assessment of this effect is crucial for a robust measurement of the large-scale clustering of galaxies. This window effect is a source of observational systematic error and impacts the measured galaxy clustering, especially on scales comparable to survey size.

We follow a similar approach to that of Chon et al. (2004) to model the window function effect on the theoretical power spectrum C_ℓ rather than correcting the measured pseudo-power spectrum from data. First, we use HEALPIX to compute the pseudo-power spectrum of the window $\hat{C}_\ell^{\text{window}}$, which is defined by a mask file in ring ordering format with NSIDE= 256. Then, we transform it to correlation function by,

$$\omega^{\text{window}}(\theta) = \frac{1}{4\pi} \sum_{\ell} (2\ell+1) \hat{C}_\ell^{\text{window}} P_\ell(\cos \theta). \quad (14)$$

Next, we normalize ω^{window} such that it is normalized to one at $\theta = 0$. Finally, we multiply the theory correlation function by ω^{window} and transform the result back to ℓ -space,

$$\hat{\omega}^{\text{model}} = \omega^{\text{model}} \omega^{\text{window}} \quad (15)$$

$$\hat{C}_\ell^{\text{model}} = 2\pi \int d\theta \hat{\omega}^{\text{model}}(\theta) P_\ell(\cos \theta). \quad (16)$$

The integral of the galaxy density contrast δ on the footprint is bound to zero, which is often referred to as the *Integral Constraint*. We account for this effect in the modeling by,

$$\hat{C}_\ell^{\text{model,IC}} = \hat{C}_\ell^{\text{model}} - \hat{C}_{\ell=0}^{\text{model}} \left(\frac{\hat{C}_\ell^{\text{window}}}{\hat{C}_{\ell=0}^{\text{window}}} \right) \quad (17)$$

Fig. 5 shows the mean measured power spectrum of 1000 lognormal density fields (dashed) and best fit theory prediction. Light and dark shades represent the 68% error on the mean and one single realization, respectively. DESI footprint mask is applied to the mocks, and even though DESI covers around 40% of the sky, but the window effect is affecting modes down to $\ell = 200$. On the other hand, integral constraint only alters the power in the first two bins.

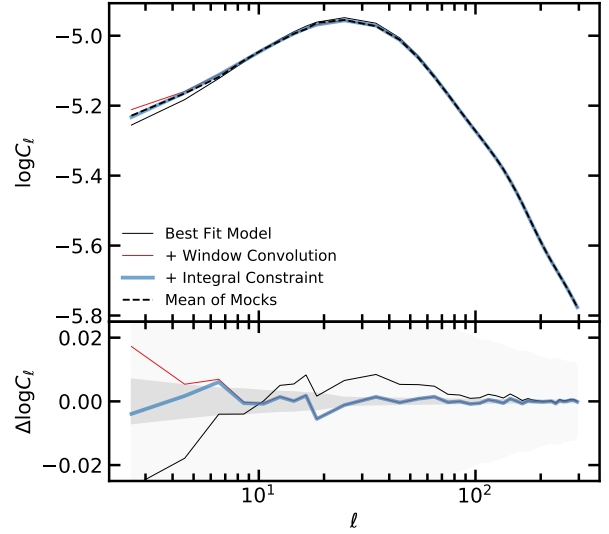


Figure 5. Mean power spectrum of 1000 mocks with $f_{\text{NL}} = 0$ and best fit theoretical prediction after accounting for various theoretical systematic effects, namely survey geometry effect and integral constraint. Dark and light shades represent 1σ error on the mean and one realization, respectively. Bottom panel shows the residual relative to the mean of mocks. No imaging systematic effects are added to these mocks.

3.3 Parameter estimation

Signature of local PNG is unique and cannot be reproduced with other cosmological parameters. We allow three parameters to vary; f_{NL} , shotnoise, and bias at $z = 0$. Throughout this manuscript, we bin each mode with $\Delta\ell = 2$ between $\ell = 2$ and 20 and $\Delta\ell = 10$ from $\ell = 20$ to 300, while weighting each mode by $2\ell + 1$. We also find that the distribution of power spectrum at the lowest bin, $2 \leq \ell < 12$, is not Gaussian and its standard deviation varies significantly from mocks with $f_{\text{NL}} = 0$ to 76.9 (see, Fig. 4). Therefore, we attempt to fit $\log C_\ell$ to make our constraints insensitive to the choice of covariance matrix. The parameter f_{NL} is constrained by maximizing a posterior defined as,

$$-2 \ln \mathcal{L} = (\log C(\Theta) - \log \hat{C})^\dagger \mathbb{C}^{-1} (\log C(\Theta) - \log \hat{C}) + \chi_{\text{priors}}^2, \quad (18)$$

where Θ represents the parameters, f_{NL} , bias at $z = 0$, and shotnoise, all of which are associated with a flat prior, χ_{priors}^2 ; $C(\Theta)$ is the (binned) theoretical power spectrum including the effects for survey geometry and integral constraint; \hat{C} is the (binned) measured power spectrum; and \mathbb{C} is the covariance matrix constructed from simulations.

3.4 Characterization of residual systematic error

We use the diagnostic tests first applied to SDSS data in Rezaie et al. (2021) based on cross power spectrum between galaxy density field and imaging maps and mean density contrast as a function of imaging properties to quantify the significance of imaging systematic effects.

3.4.1 Cross Spectrum

Taking $C_\ell^{g,x}$ as the cross power spectrum between galaxy density contrast field and imaging map, one can normalize this quantity by

⁴ github.com/xfangcosmo/FFTLog-and-beyond

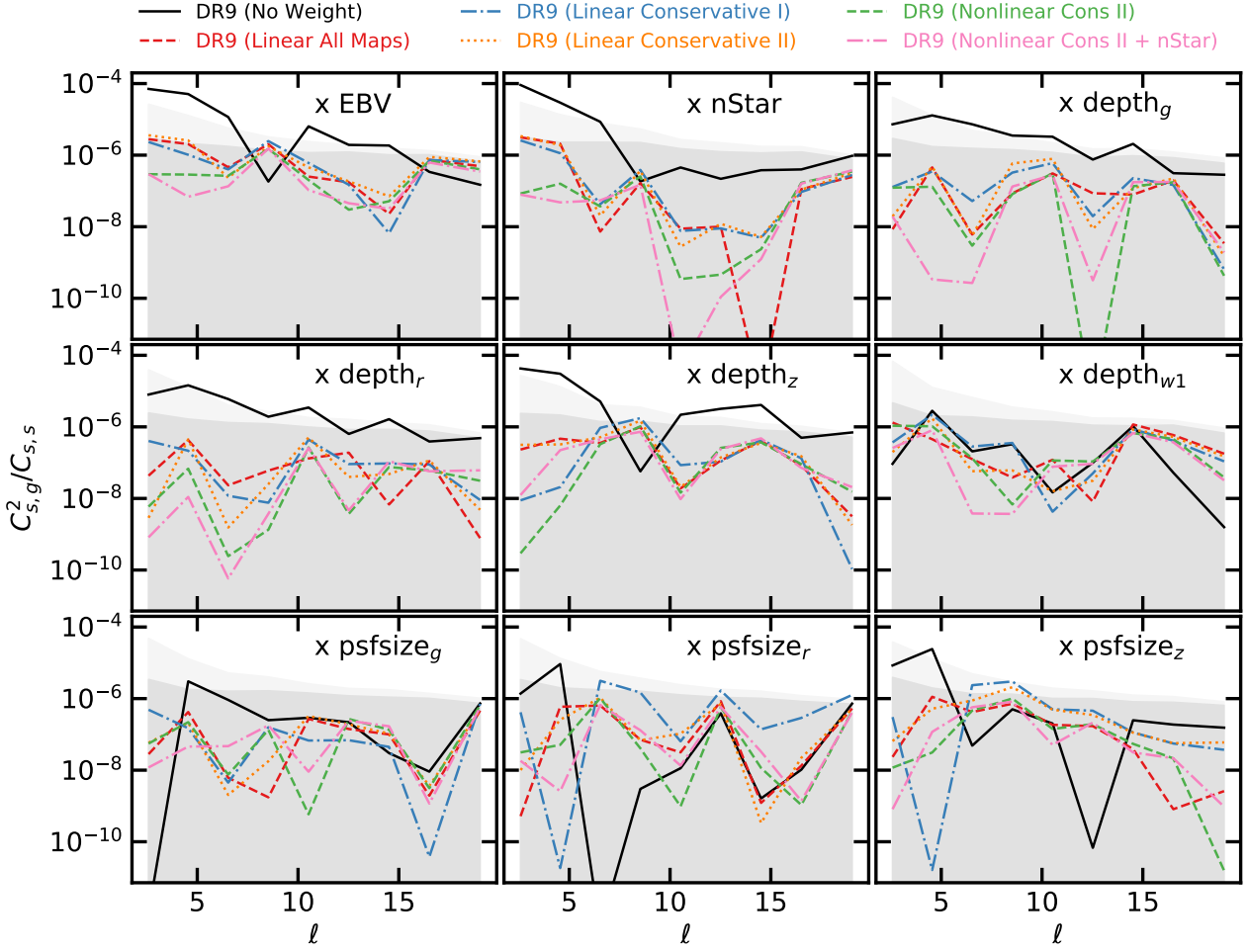


Figure 6. Residual systematic fluctuations of DR9 LRGs against imaging maps. Left: cross spectrum. Right: mean density contrast. Shades represent 1σ dispersion of 1000 clean mocks with and without f_{NL} . Solid curve shows the data before applying any weights, while the red dashed shows the data with linear all maps, and blue dot-dashed shows the data with linear cons I, and orange dotted curve shows linear cons II. The nonlinear models are shown with blue dashed and red dot-dashed.

auto power spectrum of imaging map itself:

$$\hat{C}_{x,\ell} = \frac{(\hat{C}_\ell^{g,x})^2}{\hat{C}_\ell^{x,x}}, \quad (19)$$

and then construct a vector from cross spectra against all other imaging maps:

$$\hat{C}_{X,\ell} = [\hat{C}_{x_1,\ell}, \hat{C}_{x_2,\ell}, \hat{C}_{x_3,\ell}, \dots, \hat{C}_{x_9,\ell}]. \quad (20)$$

Finally, cross power spectrum χ^2 can be defined as,

$$\chi^2 = C_{X,\ell}^T C_X^{-1} C_{X,\ell}, \quad (21)$$

where covariance matrix $C_X = \langle C_{X,\ell} C_{X,\ell'} \rangle$ is constructed from mocks without systematic effects. This statistics is measured for every mock realization with the leave-one-out technique to construct a histogram, which is then compared to the χ^2 value observed from the DR9. Fig. 7 (top) shows the measured C_X the DR9 sample before and after applying various imaging weights, relative to that of the mocks with $f_{\text{NL}} = 0$. The dispersions of mocks with and without PNG are shown with the shade regions for comparison. We bin the C_X measurements from $\ell = 2$ to 20 with $\Delta\ell = 2$. The mean and standard deviation of $\hat{C}_{X,\ell}$ for 1000 mocks with and without f_{NL}

are shown in Fig. 7. Extinction and stellar density have the highest cross power spectrum, and then depth in the z band. After applying the first version of weights with linear conservative I which includes extinction and depth-z, the cross power increases against psfsize in the r band. This indicates that only two maps are not sufficient to null out all of the cross correlations. With linear model there is residual power against extinction, depth-z, and psfsize-z; therefore, we apply weights based on a nonlinear model to account for more complex systematic effects.

Fig. 8 (top) shows the histogram of cross spectrum χ^2 from mocks with and without f_{NL} . Comparing with the data, the residual is 20014.8 before correction, and after applying the first set of weights, it reduces to 375.1 with p-value XXX. Adding psfsize-z, the linear model reduces the error down to 195.9 (p-value = XXX). Although using all maps gives the lowest error i.e., 129.2, but it could potentially lead to over-fitting true clustering given how correlated the imaging maps are (see, Fig. 3). On the other hand, the nonlinear method with three maps yields a χ^2 value of 79.3 and p-value of XXX, and adding the stellar density map reduces the error to 70.9 (p-value=XXX). This test clearly shows that a nonlinear approach is desired to get a null test. We further test the stability of our results by extending the highest mode from $\ell = 20$ to 100, or

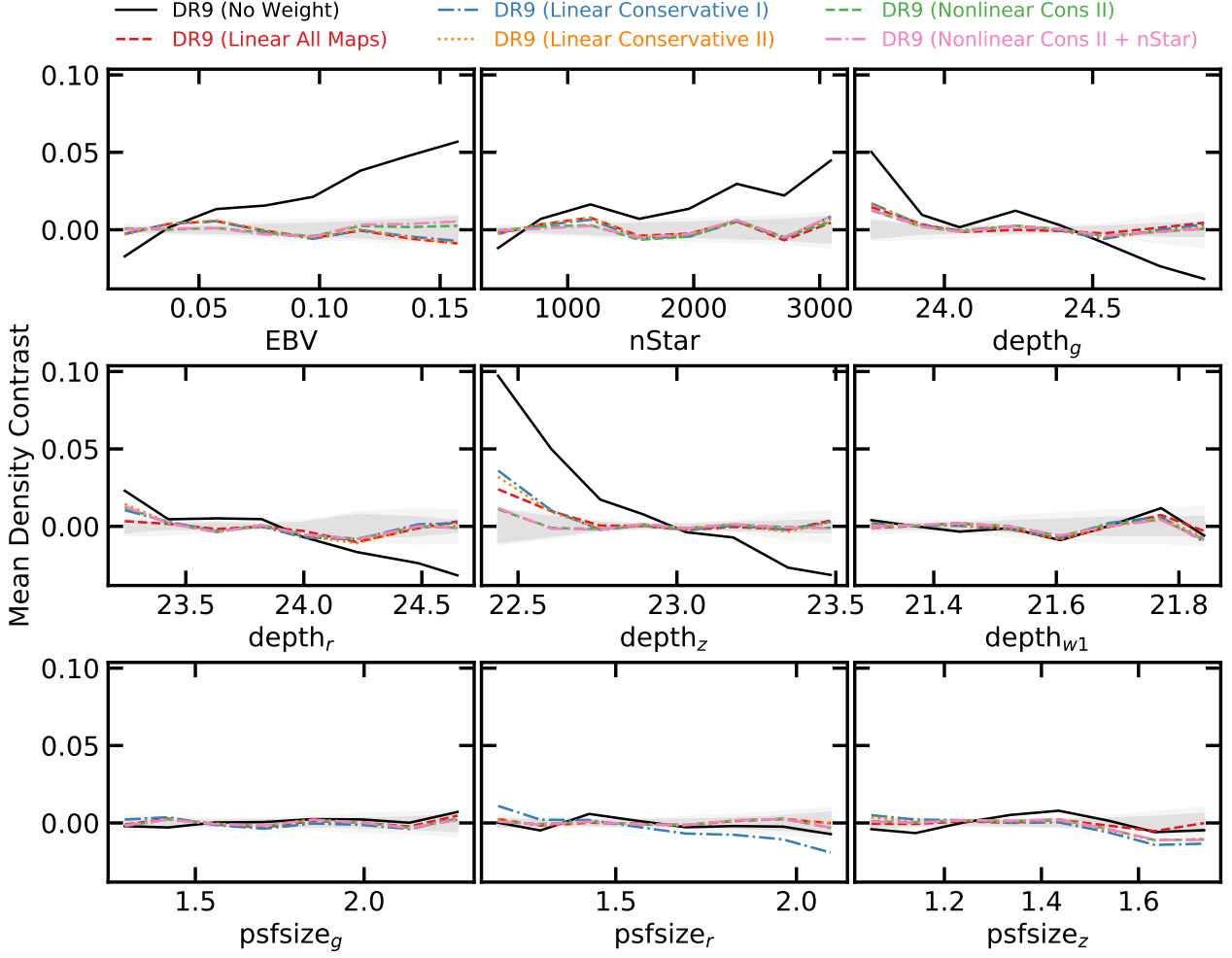


Figure 7. Residual systematic fluctuations of DR9 LRGs against imaging maps. Left: cross spectrum, Right: mean density contrast. Shades represent 1σ dispersion of 1000 clean mocks with and without f_{NL} . Solid curve shows the data before applying any weights, while the red dashed shows the data with linear all maps, and blue dot-dashed shows the data with linear cons I, and orange dotted curve shows linear cons II. The nonlinear models are shown with blue dashed and red dot-dashed.

fluctuations over scales as small as 1.8 degrees (see, Fig. 9). The solid line shows how the median of 1000 mocks changes as the highest ℓ increases from 20 to 100. The red circles show the chi2 for the linear approach with three maps and the blue crosses show the chi2 for the nonlinear approach with three maps.

3.4.2 Mean Density

In the absence of systematic error, the integral of mean density contrast over the footprint should be zero. As an alternative test, we calculate the histogram of the density contrast field relative to each imaging map.

$$\delta_x = (\hat{\rho})^{-1} \frac{\sum_i \rho_i f_{pix,i}}{\sum_i f_{pix,i}}, \quad (22)$$

where the summations are over pixels in each bin of imaging map x . Similarly, we construct the mean density contrast vector against all imaging maps,

$$\delta_X = [\delta_{x_1}, \delta_{x_2}, \delta_{x_3}, \dots, \delta_{x_9}], \quad (23)$$

and the total residual error as,

$$\chi^2 = \delta_X^T \mathbb{C}_\delta^{-1} \delta_X, \quad (24)$$

where the covariance matrix $\mathbb{C}_\delta = \langle \delta_X \delta_X^T \rangle$ is constructed from mocks without systematic effects. Fig. 7 (bottom) shows the mean density contrast for the DR9 LRG sample. The shades represent the 1σ level fluctuations observed in 1000 clean mocks with $f_{NL} = 0$ and 76.92. Before treatment (solid) shows strong correlation around 10% against depth in the z band which is consistent with the cross power spectrum. Beside that, there are strong positive trends against extinction and stellar density at about 5 – 6%. The linear model is able to mitigate most of the systematic effects with only the extinction and depth-z maps as input, however a new trend appears against psfsize-r which is indicative of psfsize dependence in the sample. This finding is in agreement with the cross power spectrum. Even after applying the linear weights there is some residual against depth-z at around 2%, which indicates the systematic effects might be more complex than what can be removed using a linear model. Nonlinear model with three maps (or four maps including the stellar density) is capable of reducing the fluctuations below 2%.

Fig. 8 (bottom) shows the mean density χ^2 observed in the

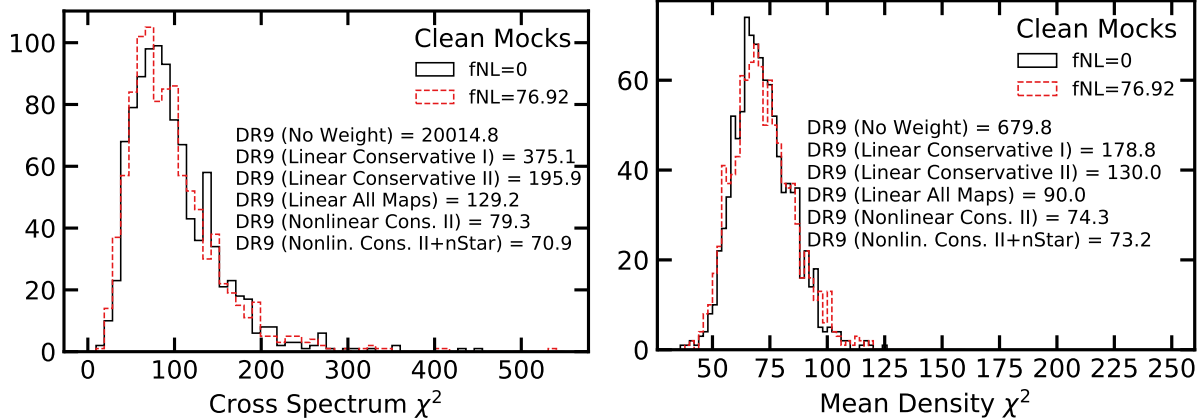


Figure 8. Left: Cross power spectrum χ^2 diagnostic. Right: Mean density contrast diagnostic. The values observed in DR9 before and after linear and nonlinear treatments are quoted and the histograms are constructed from 1000 realizations of clean mocks with $f_{NL} = 0$ and 76.92.

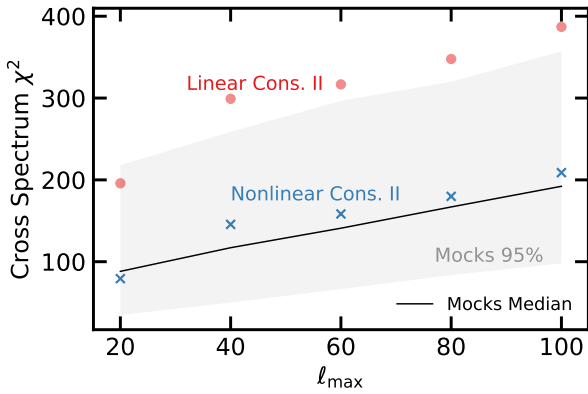


Figure 9. Cross Spectrum χ^2 for DR9 LRG density and imaging maps with linear and nonlinear cleaning (both with conservative II maps) as a function of the highest mode l_{max} while the lowest mode is fixed at $l_{min} = 2$. Solid curve and shade represent the median estimate and 68% confidence constructed from $f_{NL} = 0$ mocks.

mocks vs DR9 sample before and after applying imaging weights. Linear weights with two maps reduce the chi-2 value from 679.8 (before) to 178.8. The p-value is indicative of remaining systematic effects. Adding psfsize-r does not help much with the p-value even though it reduces the chi-2 to 130. Using all maps with the linear model gives a more reasonable value however it leaves the analysis susceptible to over-fitting true clustering signal. With nonlinear approach two maps as input, the chi-2 is reasonable 74.3 with p-value XXX, and adding the stellar map does not change the p-value much, indicating the trend against stellar density can be explained with the extinction to a great extend.

4 RESULTS

This sections presents the constraint on f_{NL} from the DR9 LRG sample. The robustness of constraints are tested against various assumptions and details in survey mask, imaging weights, and calibration of data. The default analysis uses the covariance from $f_{NL} = 0$ mocks. We also validate the modeling pipeline and characterize the amount of mitigation bias introduced in f_{NL} after cleaning for systematics.

4.1 Lognormal Mocks

Corner plots of the PNG parameter f_{NL} and bias coefficient are shown in Fig. 10 for fitting the mean power spectrum of mocks, with and without f_{NL} . Best fit estimates, marginalized mean, 1σ and 2σ confidence intervals are summarized in Tab. 2. Fig 10 (right) shows confidence contours for different combinations of target variable (e.g., either power spectrum or its log transform) and covariance matrix. First we attempt to understand the impact of covariance on confidence intervals. We fit the mean power spectrum of $f_{NL} = 76.9$ mocks or its log transformation using covariance matrices constructed from the same set of mocks or from the $f_{NL} = 0$ mocks. When covariance is consistent with mean, the difference between fitting power spectrum and log of it is only 2%. If a wrong covariance is used for the log power, the effect is only 7%. However, when mean power spectrum of the $f_{NL} = 76.9$ mocks is fit using the covariance matrix estimated from the $f_{NL} = 0$ mocks, the constraints improve by a factor of 5, simply due to a false higher signal to noise ratio. Therefore, we argue that fitting logarithm of power spectrum would remove the need for having f_{NL} -dependent covariance matrices and make the constraints less sensitive to covariance construction. Fig. 10 (left) shows the confidence contours for $f_{NL} = 0$ mocks when fit is done to the log of mean spectra of $f_{NL} = 0$ mocks for the different regions. We find that the underlying true f_{NL} value is recovered within 2σ confidence. **Add a paragraph for the constraining power vs fsky.**

Fig 11 shows the best fit estimates for b vs f_{NL} for $f_{NL} = 0$ and $= 76.92$ mocks in the left and right, respectively. Truth values are represented via the dotted lines. The points are color-coded with the minimum χ^2 from fit for each realization. The histograms of best fit f_{NL} estimates are plotted in the background. We obtain $f_{NL} = MU \pm STD$ and $= MU \pm STD$ for the left and right panels, respectively.

With template based mitigation, the measured power spectrum is biased and the amount of bias depends on the number of input templates. We use a linear model with the set of conservative II maps to simulate imaging systematics in our lognormal density fields. Then, we apply the cleaning method based on nonlinear model with Conservative II, Conservative II + nStar, or All Maps + nStar sets of imaging maps to both set of mocks; with or without systematic effects (dashed or solid), and with and without f_{NL} . The marginalized mean, confidence intervals, and best fit estimates are presented in Tab 3. This test indicates that as more maps are

Table 2. Maximum-A-Posteriori (MAP) and marginalized mean estimates for f_{NL} from fitting the mean power spectrum of the mocks. Degree of freedom is 34 (37 data points - 3 parameters).

True f_{NL}	Footprint	Observable	f_{NL}				χ^2
			Best fit	Mean	68% CL	95% CL	
76.92	DESI	$\log C_\ell$	77.67	77.67	$77.17 < f_{\text{NL}} < 78.16$	$76.71 < f_{\text{NL}} < 78.64$	38.8
76.92	DESI	C_ℓ	77.67	77.65	$77.17 < f_{\text{NL}} < 78.14$	$76.70 < f_{\text{NL}} < 78.60$	39.0
76.92	DESI	$\log C_\ell + f_{\text{NL}} = 0 \text{ cov}$	77.70	77.71	$77.25 < f_{\text{NL}} < 78.17$	$76.81 < f_{\text{NL}} < 78.63$	39.9
76.92	DESI	$C_\ell + f_{\text{NL}} = 0 \text{ cov}$	77.03	77.02	$76.93 < f_{\text{NL}} < 77.12$	$76.83 < f_{\text{NL}} < 77.22$	207.6
0	DESI	$\log C_\ell$	0.36	0.36	$0.06 < f_{\text{NL}} < 0.65$	$-0.23 < f_{\text{NL}} < 0.94$	35.7
0	DECaLS North	$\log C_\ell$	0.07	0.06	$-0.47 < f_{\text{NL}} < 0.60$	$-1.00 < f_{\text{NL}} < 1.12$	26.7
0	DECaLS South	$\log C_\ell$	0.67	0.67	$0.13 < f_{\text{NL}} < 1.22$	$-0.40 < f_{\text{NL}} < 1.75$	34.3
0	BASS+MzLS	$\log C_\ell$	0.83	0.82	$0.25 < f_{\text{NL}} < 1.40$	$-0.31 < f_{\text{NL}} < 1.96$	39.4

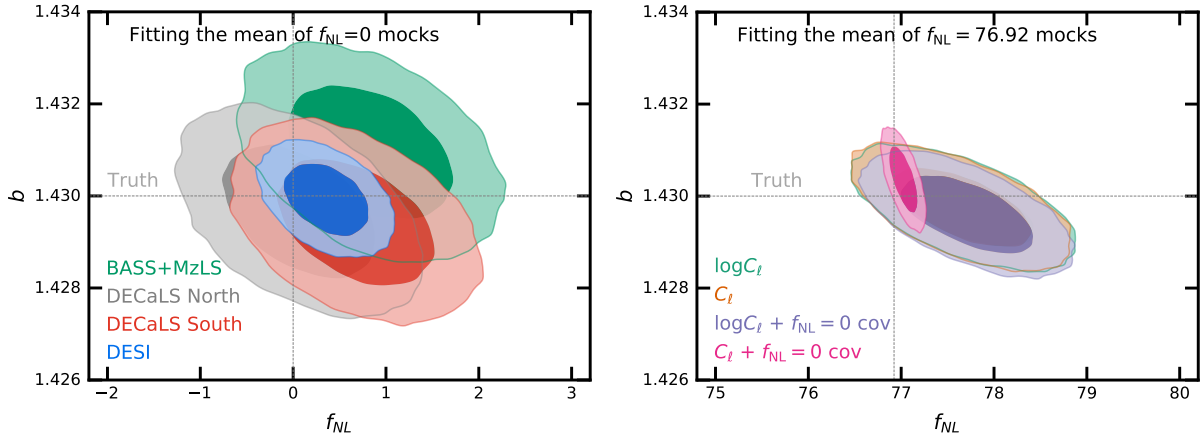


Figure 10. Top: 68% and 95% confidence contours for $f_{\text{NL}} = 0$ (left) and 76.92 (right) mocks. Using the $\log C_\ell$ fitting yield constraints that are insensitive to the covariance used. Bottom: best fit estimates from fitting 1000 lognormal mocks with $f_{\text{NL}} = 0$ (left) and 76.92 (right) in the DESI footprint. The truth values are represented by vertical and horizontal lines.

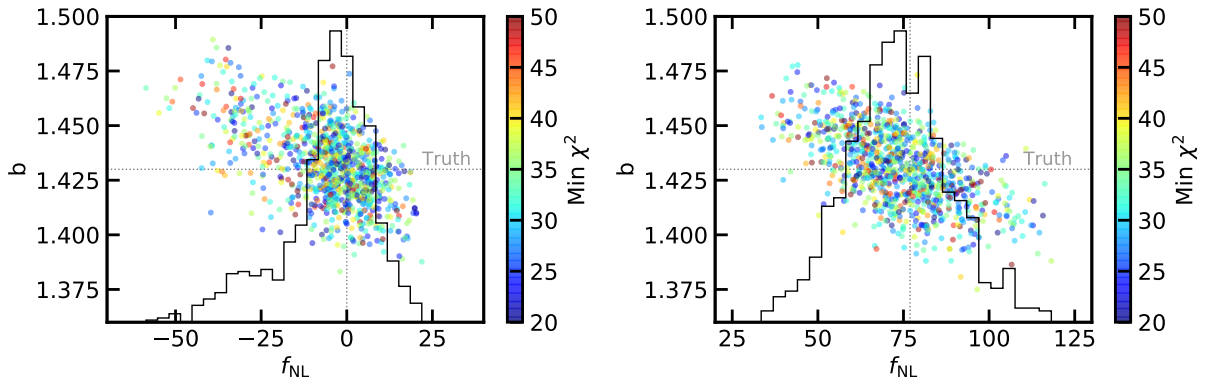


Figure 11. Top: 68% and 95% confidence contours for $f_{\text{NL}} = 0$ (left) and 76.92 (right) mocks. Using the $\log C_\ell$ fitting yield constraints that are insensitive to the covariance used. Bottom: best fit estimates from fitting 1000 lognormal mocks with $f_{\text{NL}} = 0$ (left) and 76.92 (right) in the DESI footprint. The truth values are represented by vertical and horizontal lines.

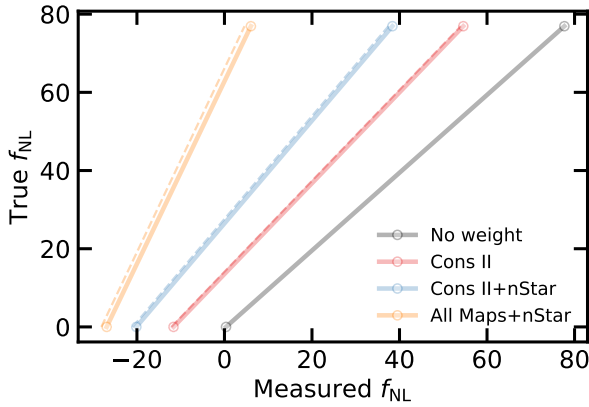
input to the nonlinear model, more power is removed, and thus the constraints are systematically shifted to lower f_{NL} values. Fig 12 shows the true f_{NL} value and the measured f_{NL} value from fitting the mean of mocks. The results for the contaminated mocks before cleaning (No weight) is not shown for clarity. From this graph, then a pair of linear coefficients are to be found for mapping measured f_{NL} to true f_{NL} values. At the first iteration, we think these coefficients should be applied to the values presented in Tab 4.

4.2 DR9 LRGs

Fig. 13 shows the measured power spectrum of DR9 LRGs with different imaging weights, the best fit theory curves, and the mean and 1σ error from the $f_{\text{NL}} = 0$ lognormal mocks. Power spectra are similar with differences less than 1% for small scales ($\ell > 2$), and as we go to larger scales, the differences become more significant. There is a little difference between linear cons II and linear all maps. This proves that our feature selection procedure has worked

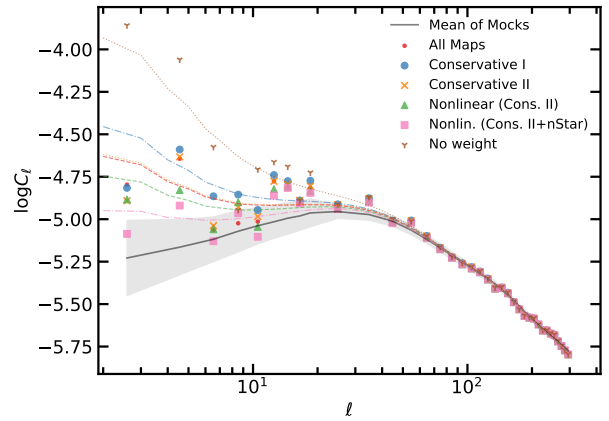
Table 3. Best fit and marginalized estimates for f_{NL} from fitting the mean power spectrum of the mocks before and after applying imaging weights.

Mock	Method	f_{NL}					χ^2
		Best fit	Mean	68% CL	95% CL		
0	No Weight	0.36	0.36	$0.06 < f_{\text{NL}} < 0.65$	$-0.23 < f_{\text{NL}} < 0.94$		35.7
0	ConsII	-11.64	-11.65	$-12.00 < f_{\text{NL}} < -11.30$	$-12.34 < f_{\text{NL}} < -10.97$		86.8
0	ConsII+nStar	-20.14	-20.13	$-20.44 < f_{\text{NL}} < -19.82$	$-20.74 < f_{\text{NL}} < -19.52$		472.8
0	All Maps+nStar	-26.91	-26.92	$-27.16 < f_{\text{NL}} < -26.68$	$-27.39 < f_{\text{NL}} < -26.46$		5481.0
Contaminated 0	ConsII	-12.12	-12.13	$-12.48 < f_{\text{NL}} < -11.78$	$-12.83 < f_{\text{NL}} < -11.44$		94.0
Contaminated 0	ConsII+nStar	-20.97	-20.98	$-21.28 < f_{\text{NL}} < -20.67$	$-21.58 < f_{\text{NL}} < -20.37$		556.3
Contaminated 0	All Maps+nStar	-28.13	-28.13	$-28.36 < f_{\text{NL}} < -27.90$	$-28.59 < f_{\text{NL}} < -27.67$		6760.5
76.92	No Weight	77.67	77.67	$77.17 < f_{\text{NL}} < 78.16$	$76.71 < f_{\text{NL}} < 78.64$		38.8
76.92	ConsII	54.57	54.57	$54.14 < f_{\text{NL}} < 55.01$	$53.72 < f_{\text{NL}} < 55.45$		603.5
76.92	ConsII+nStar	38.38	38.38	$37.99 < f_{\text{NL}} < 38.78$	$37.60 < f_{\text{NL}} < 39.16$		537.0
76.92	All Maps+nStar	6.04	6.04	$5.72 < f_{\text{NL}} < 6.36$	$5.41 < f_{\text{NL}} < 6.67$		694.0
Contaminated 76.92	ConsII	54.01	54.00	$53.57 < f_{\text{NL}} < 54.44$	$53.15 < f_{\text{NL}} < 54.86$		588.0
Contaminated 76.92	ConsII+nStar	37.48	37.49	$37.09 < f_{\text{NL}} < 37.88$	$36.70 < f_{\text{NL}} < 38.27$		510.7
Contaminated 76.92	All Maps+nStar	4.59	4.58	$4.26 < f_{\text{NL}} < 4.90$	$3.95 < f_{\text{NL}} < 5.22$		649.7

**Figure 12.** True f_{NL} vs measured f_{NL} from mocks with (dashed) and without systematics (solid).

to identify the important maps. Comparing linear cons I to linear cons II, modes with $6 \leq \ell < 10$ are different, indicating scales where psfsize-r is affecting the signal. Comparing nonlinear cons II to linear cons II, modes at the second bin ($4 \leq \ell < 6$) are very different, indicating the nonlinear approach is more flexible to reduce fluctuations on small scales as well large scales.

f_{NL} constraints from DR9 LRG sample is summarized in Table 4. First, we focus on the DESI footprint and then compare constraints obtained from each sub-survey. Fig 14 shows the 2D constraints with 68% and 95% confidence on f_{NL} and b for the DESI footprint from the DR9 sample before (no weight) and after applying different cleaning schemes. No weight constraint at 68% is $98.14 < f_{\text{NL}} < 132.89$ with a best fit of 113.18 and marginalized mean of 115.49, and is more than 2σ off from zero. Applying imaging weights shifts constraints to lower f_{NL} values, and b is slightly pulled upward since excess clustering due to systematics is removed. Using all maps with the linear model does not change the results, showing that three maps are sufficient at the linear level to mitigate systematics. As an alternative, using a nonlinear model with three maps shows around 1σ shift, with 68% confidence at $18.91 < f_{\text{NL}} < 40.59$, inconsistent with zero for more than 2σ . Adding a template for the local stellar density shift constraints by 1σ , making it consistent with zero. As the most rigorous approach, using all maps and stellar density included results in more than 2σ shift. We emphasize that these shifts to lower f_{NL} are somewhat ex-

**Figure 13.** Measured power spectrum of the DR9 LRG sample before and after correcting for systematics with their corresponding best fit theory predictions. The shade represents 1σ error constructed from the $f_{\text{NL}} = 0$ mocks.

pected as more input maps results in regressing more modes from cosmological clustering signal. Therefore, we use lognormal mocks to calibrate the amount of signal that is removed in each case and attempt to undo the effect.

4.2.1 Robustness tests

We also evaluate the robustness of constraints against various cuts and configurations. First, we compare how constraints from whole DESI footprint compares to those from each survey individually, namely BASS+MzLS, DECaLS North, and DECaLS South. Fig. 15 shows 68% and 95% confidence on f_{NL} and b from each individual survey or all combined as DESI. Constraints from all surveys are consistent and agree with each other within 68%. Both BASS+MzLS and DECaLS South are consistent with zero PNG, but DECaLS North deviates from zero at more than 2σ . Adding the stellar density template does not change constraints from BASS+MzLS much, but it shifts DECaLS North and DECaLS South by 0.5σ and σ , respectively. This might indicate that there are some unresolved issues with stellar contamination in DECaLS North and DECaLS South. We note that differences are more significant when all maps and stellar density are used as input. This is expected as more maps mean the model has more freedom to take out clustering modes.

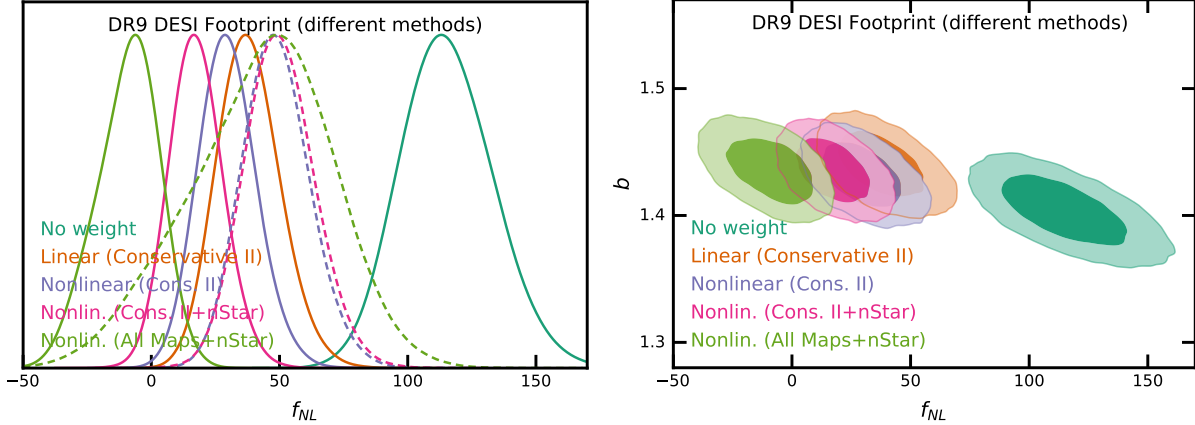


Figure 14. 1D and 2D f_{NL} constraints from DR9 LRG sample before and after applying linear and nonlinear cleaning methods.

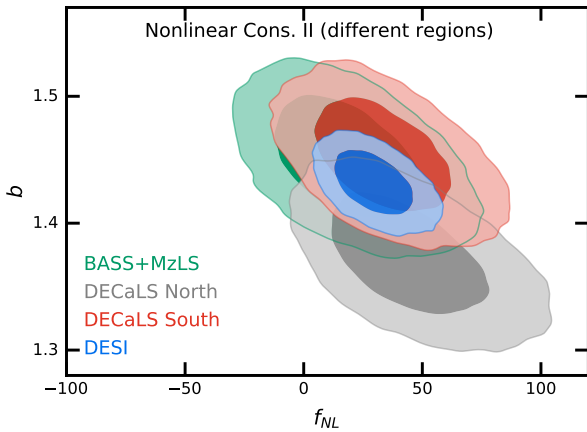


Figure 15. DR9 constraints. Each individual imaging survey versus the whole DESI footprint.

- **Pixel completeness** We remove pixels with low completeness from the DESI footprint by applying $f_{\text{pix}} > 0.5$, and find that the impact is negligible. Specifically, the cut removes .6% survey area and causes best fit f_{NL} shifts only around 2%, from 28.58 to 28.07, see *comp cut* Table 4. When investigated this impact on each region separately, BASS+MzLS increases around 10%, DECaLS North decreases 1%, and DECaLS South decreases around 5%.
- **Imaging quality** We remove pixels with poor imaging from the DESI footprint by applying the following cuts on imaging properties; $E[B - V] < 0.1$, $n\text{Star} < 3000$, $\text{depth}_g > 23.2$, $\text{depth}_r > 22.6$, $\text{depth}_z > 22.5$, $\text{psfsize}_g < 2.5$, $\text{psfsize}_r < 2.5$, and $\text{psfsize}_z < 2$. Overall the constraints are consistent despite best fit and marginalized mean estimates shift. Quantitatively, we lose about 8.2% survey area, and the best fit f_{NL} estimate changes about 2% from 28.58 to 29.16. See *imag cut* in Table 4. For BASS+MzLS only, the imaging cut increases the best fit by 62% from 15.43 to 25.03. For DECaLS North and DECaLS South, the best fit increases by 5% and 15% respectively.
- **Covariance** We now use the mocks with $f_{\text{NL}} = 76.92$ to construct a covariance matrix, and with the new covariance we observe a 12% increase in the f_{NL} constraint uncertainties and 11% increase in the best fit estimate of f_{NL} .
- **Lowest ℓ** We decrease the largest mode (or increase the lowest ℓ) used in estimating the best fit and 68% confidence intervals. Fig. 16

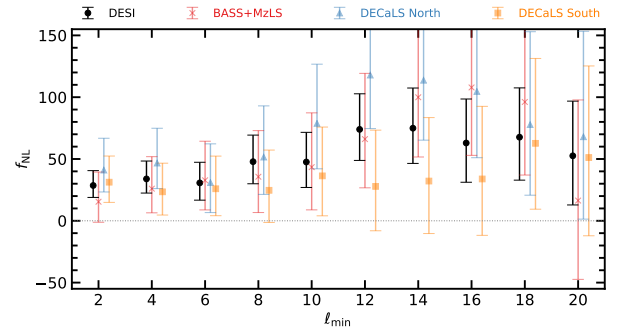


Figure 16. Robustness of DR9 constraints to the largest scale (lowest ℓ mode) used in MCMC regression. Points represent marginalized mean estimates of f_{NL} and errorbars represent 68% confidence.

illustrates the results for the DESI footprint and how they compared to BASS+MzLS, DECaLS North, or DECaLS South only results. Points represent marginalized mean estimates of f_{NL} and errorbars represent 68% confidence from MCMC results. Overall we find that the constraints are robust against the largest mode.

- **External maps** We also derive imaging weights using additional external maps for the neutral hydrogen column density (HI) and magnitude calibration errors in the z band (CALIBZ). With the new weights, we find the best fit estimates increase from 41.02 to 55.46 for DECaLS North and from 31.24 to 33.79 for DECaLS South.
- **Declination cut** Our default analysis do not use the spurious islands in DECaLS North and DECaLS South below DEC = -30 to avoid potential calibration issues. **PANASTARS are used for calibration below DEC of -30.** Without these cuts, best fit f_{NL} estimates increase from 31.24 to 43.79 for DECaLS South and decrease from 41.02 to 41.05. This indicates that indeed there is an issue with DECaLS South below DEC of -30.

Overall we find that the declination cut is necessary for DECaLS South, while adding external templates for HI and CALIBZ, using a different covariance, or applying imaging and completeness cuts do not alter the constraints significantly.

4.2.2 Calibrated constraints

Fig 12 is adapted to debias f_{NL} constraints. With the corrections applied, we obtain $36.07(25.03) < f_{\text{NL}} < 61.44(75.64)$ for non-

Table 4. Maximum-A-Posteriori (MAP) and marginalized mean estimates for f_{NL} from fitting power spectrum of DR9 LRGs before and after correcting for systematics. Degree of freedom is 34 (37 data points - 3 parameters).

Footprint	Method	f_{NL}				χ^2
		Best fit	Mean	68% CL	95% CL	
DESI	No Weight	113.18	115.49	$98.14 < f_{\text{NL}} < 132.89$	$83.51 < f_{\text{NL}} < 151.59$	44.4
DESI	Linear (All Maps)	36.05	37.72	$26.13 < f_{\text{NL}} < 49.21$	$16.31 < f_{\text{NL}} < 62.31$	41.1
DESI	Linear (Conservative I)	49.58	51.30	$38.21 < f_{\text{NL}} < 64.33$	$27.41 < f_{\text{NL}} < 78.91$	38.8
DESI	Linear (Conservative II)	36.63	38.11	$26.32 < f_{\text{NL}} < 49.86$	$16.36 < f_{\text{NL}} < 63.12$	39.6
DESI	Nonlinear (Cons. II)	28.58	29.79	$18.91 < f_{\text{NL}} < 40.59$	$9.47 < f_{\text{NL}} < 52.73$	34.6
DESI	Nonlin. (Cons. II+nStar)	16.63	17.52	$7.51 < f_{\text{NL}} < 27.53$	$-1.59 < f_{\text{NL}} < 38.49$	35.2
DESI	Nonlin. (All Maps+nStar)	-5.87	-9.19	$-21.45 < f_{\text{NL}} < 2.40$	$-33.81 < f_{\text{NL}} < 12.06$	39.5
DESI (imag. cut)	Nonlin. (Cons. II)	29.16	30.57	$19.05 < f_{\text{NL}} < 42.18$	$9.01 < f_{\text{NL}} < 54.81$	35.8
DESI (comp. cut)	Nonlin. (Cons. II)	28.07	29.48	$18.38 < f_{\text{NL}} < 40.50$	$8.81 < f_{\text{NL}} < 53.10$	34.5
DESI	Nonlin. (Cons. II)+ $f_{\text{NL}} = 76.92$ Cov	31.62	33.11	$20.94 < f_{\text{NL}} < 45.24$	$10.56 < f_{\text{NL}} < 59.16$	33.5
BASS+MzLS	Nonlin. (Cons. II)	15.43	19.01	$-1.17 < f_{\text{NL}} < 39.43$	$-19.19 < f_{\text{NL}} < 63.56$	35.6
BASS+MzLS	Nonlin. (Cons. II+nStar)	13.12	15.39	$-4.59 < f_{\text{NL}} < 35.56$	$-24.88 < f_{\text{NL}} < 59.31$	34.7
BASS+MzLS	Nonlin. (All Maps+nStar)	-3.73	-6.34	$-27.11 < f_{\text{NL}} < 13.75$	$-47.44 < f_{\text{NL}} < 33.94$	36.8
BASS+MzLS (imag. cut)	Nonlin. (Cons. II)	25.03	29.12	$6.16 < f_{\text{NL}} < 52.44$	$-14.22 < f_{\text{NL}} < 80.54$	36.2
BASS+MzLS (comp. cut)	Nonlin. (Cons. II)	16.99	20.90	$0.26 < f_{\text{NL}} < 41.76$	$-18.30 < f_{\text{NL}} < 67.12$	35.8
DECaLS North	Nonlin. (Cons. II)	41.02	44.89	$23.33 < f_{\text{NL}} < 66.78$	$4.96 < f_{\text{NL}} < 93.02$	41.1
DECaLS North	Nonlin. (Cons. II+CALIBZ+HI)	55.46	60.44	$36.78 < f_{\text{NL}} < 84.05$	$17.86 < f_{\text{NL}} < 112.81$	38.4
DECaLS North	Nonlin. (Cons. II+nStar)	31.45	34.78	$14.14 < f_{\text{NL}} < 55.79$	$-5.81 < f_{\text{NL}} < 80.80$	41.2
DECaLS North	Nonlin. (All Maps+nStar)	0.81	-5.68	$-29.73 < f_{\text{NL}} < 16.71$	$-53.15 < f_{\text{NL}} < 36.19$	45.1
DECaLS North + islands	Nonlin. (Cons. II)	41.05	44.82	$23.58 < f_{\text{NL}} < 66.08$	$6.40 < f_{\text{NL}} < 91.42$	40.7
DECaLS North (imag. cut)	Nonlin. (Cons. II)	43.27	48.39	$24.60 < f_{\text{NL}} < 72.50$	$4.71 < f_{\text{NL}} < 101.42$	35.1
DECaLS North (comp. cut)	Nonlin. (Cons. II)	40.55	44.63	$22.41 < f_{\text{NL}} < 67.11$	$3.95 < f_{\text{NL}} < 94.06$	41.4
DECaLS South	Nonlin. (Cons. II)	31.24	33.21	$14.89 < f_{\text{NL}} < 52.40$	$-5.11 < f_{\text{NL}} < 74.35$	30.2
DECaLS South	Nonlin. (Cons. II+CALIBZ+HI)	33.79	37.50	$17.71 < f_{\text{NL}} < 57.42$	$-0.31 < f_{\text{NL}} < 80.94$	30.8
DECaLS South	Nonlin. (Cons. II+nStar)	14.34	6.28	$-21.19 < f_{\text{NL}} < 30.01$	$-53.63 < f_{\text{NL}} < 49.51$	31.9
DECaLS South	Nonlin. (All Maps+nStar)	-36.76	-32.01	$-49.38 < f_{\text{NL}} < -13.61$	$-65.26 < f_{\text{NL}} < 7.52$	31.5
DECaLS South + DEC < -30	Nonlin. (Cons. II)	43.79	46.79	$30.16 < f_{\text{NL}} < 63.41$	$16.38 < f_{\text{NL}} < 82.72$	23.8
DECaLS South (imag. cut)	Nonlin. (Cons. II)	26.47	23.36	$3.18 < f_{\text{NL}} < 47.84$	$-57.69 < f_{\text{NL}} < 71.39$	30.0
DECaLS South (comp. cut)	Nonlin. (Cons. II)	29.62	31.76	$13.00 < f_{\text{NL}} < 51.58$	$-9.78 < f_{\text{NL}} < 74.28$	29.7

linear (conservative II), $36.88(24.87) < f_{\text{NL}} < 63.31(77.78)$ for nonlinear (conservative II + nStar), and $13.09(-15.95) < f_{\text{NL}} < 69.14(91.84)$ for nonlinear (all maps + nStar) at 68%(95%) confidence.

5 CONCLUSIONS

We have presented constraints on f_{NL} using the scale-dependent bias effect in the large-scale clustering of DESI imaging DR9 LRGs. Methods from linear and nonlinear regressions are applied for data cleaning from foreground and imaging systematic effects. Same tools are tested on lognormal density fields to evaluate the sensitivity of signal to systematic error. As summarized in Table ??, we find that fitting $\log C_\ell$ rather than C_ℓ minimizes the dependence of constraints to the choice of covariance, and we are able to recover the truth f_{NL} at 95% confidence in both simulations with and without PNG. Table ??? summarizes the constraints from mocks undergone cleaning for systematics. We find that template-based regression removes clustering and thus biased constraints are obtained. We use the mock constraints to calibrate DR9 constraints. We obtain $36.07(25.03) < f_{\text{NL}} < 61.44(75.64)$ when cleaning is performed with the nonlinear model using only three imaging maps. With more extreme cleaning using all maps and stellar density, we obtain $13.09(-15.95) < f_{\text{NL}} < 69.14(91.84)$ at 68%(95%).

Various tests are performed to assess the robustness of constraints against analysis assumptions, and the results are summarized in Table ?. We find

- constraints from individual surveys are consistent with each other

- no significant shift observed in constraints after applying imaging cut, completeness cut
- no significant shift after including additional imaging templates for hydrogen column density or calibration in the z-band.
- region below dec of -30 indicates some issues probably due to unaccounted for calibration issues
- constraints are robust against the largest scales (lowest ℓ mode) used in fitting for f_{NL} . **Some signs of systematics on $10 < \ell < 18$.**

ACKNOWLEDGEMENTS

MR is supported by XXXXXX. We acknowledge the support and resources from the Ohio Supercomputer Center (OSC; [Center 1987](#)). We would like to thank the open-source software and resources that were beneficial to this research: Pytorch, Nbodykit, HEALPix, Fitsio, Scikit-Learn, NumPy, SciPy, Pandas, IPython, Jupyter, arXiv, and GitHub.

DATA AVAILABILITY

DESI imaging DR9 catalogs are publicly available at <https://www.legacysurvey.org/dr9/>. Software for cleaning imaging data is available at <https://github.com/mehdirezaie/synnetdev>. Mock catalogs can be made available upon reasonable request.

REFERENCES

- Abbott T., et al., 2016, *Monthly Notices of the Royal Astronomical Society*, 460, 1270
- Ade P., et al., 2019, *Journal of Cosmology and Astroparticle Physics*, 2019, 056
- Aghanim N., et al., 2020, *Astronomy & Astrophysics*, 641, A6
- Akrami Y., et al., 2019, arXiv preprint arXiv:1905.05697
- Alam S., et al., 2021, *Physical Review D*, 103, 083533
- Baldauf T., Seljak U., Senatore L., 2011a, *Journal of Cosmology and Astroparticle Physics*, 2011, 006
- Baldauf T., Seljak U., Senatore L., Zaldarriaga M., 2011b, *Journal of Cosmology and Astroparticle Physics*, 2011, 031
- Bassett B. A., Tsujikawa S., Wands D., 2006, *Reviews of Modern Physics*, 78, 537
- Beutler F., et al., 2014, *Monthly Notices of the Royal Astronomical Society*, 443, 1065
- Bouwens R. J., et al., 2015, *ApJ*, 803, 34
- Castorina E., Moradinezhad Dizgah A., 2020, *J. Cosmology Astropart. Phys.*, 2020, 007
- Center O. S., 1987, Ohio Supercomputer Center, <http://osc.edu/ark:/19495/f5s1ph73>
- Chaussidon E., et al., 2022, *Monthly Notices of the Royal Astronomical Society*, 509, 3904
- Chon G., Challinor A., Prunet S., Hivon E., Szapudi I., 2004, *Monthly Notices of the Royal Astronomical Society*, 350, 914
- Coles P., Jones B., 1991, *Monthly Notices of the Royal Astronomical Society*, 248, 1
- Dalal N., Dore O., Huterer D., Shirokov A., 2008, *Physical Review D*, 77, 123514
- De Mattia A., Ruhlmann-Kleider V., 2019, *Journal of Cosmology and Astroparticle Physics*, 2019, 036
- Dey A., et al., 2018, arXiv preprint arXiv:1804.08657
- Eisenstein D. J., et al., 2001, *The Astronomical Journal*, 122, 2267
- Fang X., Krause E., Eifler T., MacCrann N., 2020, *Journal of Cosmology and Astroparticle Physics*, 2020, 010
- Fillmore J. A., Goldreich P., 1984, *Astrophysical Journal*, 281, 1
- Flaugher B., et al., 2015, *The Astronomical Journal*, 150, 150
- Gaia Collaboration et al., 2018, *A&A*, 616, A1
- Giannantonio T., Ross A. J., Percival W. J., Crittenden R., Bacher D., Kilbinger M., Nichol R., Weller J., 2014, *Physical Review D*, 89, 023511
- Gorski K. M., Hivon E., Banday A. J., Wandelt B. D., Hansen F. K., Reinecke M., Bartelmann M., 2005, *The Astrophysical Journal*, 622, 759
- Guth A. H., Kaiser D. I., 2005, *Science*, 307, 884
- Heinrich C., Doré O., 2022, in *American Astronomical Society Meeting Abstracts*. p. 202.03
- Hivon E., Gorski K. M., Netterfield C. B., Crill B. P., Prunet S., Hansen F., 2002, *The Astrophysical Journal*, 567, 2
- Ho S., et al., 2015, *J. Cosmology Astropart. Phys.*, 2015, 040
- Huterer D., Cunha C. E., Fang W., 2013, *Monthly Notices of the Royal Astronomical Society*, 432, 2945
- Kitanidis E., et al., 2020, *Monthly Notices of the Royal Astronomical Society*, 496, 2262
- Kofman L., Linde A., Starobinsky A. A., 1994, *Physical Review Letters*, 73, 3195
- Komatsu E., Spergel D. N., 2001, *Physical Review D*, 63, 063002
- Lyth D. H., Liddle A. R., 2009, *The primordial density perturbation: Cosmology, inflation and the origin of structure*. Cambridge University Press
- Merz G., et al., 2021, *Monthly Notices of the Royal Astronomical Society*, 506, 2503
- Mueller E.-M., et al., 2022, *Monthly Notices of the Royal Astronomical Society*
- Myers A. D., et al., 2022, arXiv e-prints, p. arXiv:2208.08518
- Padmanabhan N., et al., 2007, *MNRAS*, 378, 852
- Peacock J., Nicholson D., 1991, *Monthly Notices of the Royal Astronomical Society*, 253, 307
- Prakash A., et al., 2016, *The Astrophysical Journal Supplement Series*, 224, 34
- Pullen A. R., Hirata C. M., 2013, *Publications of the Astronomical Society of the Pacific*, 125, 705
- Rezaie M., et al., 2021, *Monthly Notices of the Royal Astronomical Society*, 506, 3439
- Riquelme W., et al., 2022, arXiv preprint arXiv:2209.07187
- Ross A. J., et al., 2011, *Monthly Notices of the Royal Astronomical Society*, 417, 1350
- Sabti N., Muñoz J. B., Blas D., 2021, *J. Cosmology Astropart. Phys.*, 2021, 010
- Schlegel D. J., Finkbeiner D. P., Davis M., 1998, *The Astrophysical Journal*, 500, 525
- Schmittfull M., Seljak U., 2018, *Phys. Rev. D*, 97, 123540
- Slosar A., Hirata C., Seljak U., Ho S., Padmanabhan N., 2008, *Journal of Cosmology and Astroparticle Physics*, 2008, 031
- Wang M. S., Beutler F., Bacon D., 2020, *MNRAS*, 499, 2598
- Weinberg S., 2008, *Cosmology*. OUP Oxford
- Weinberg D. H., Mortonson M. J., Eisenstein D. J., Hirata C., Riess A. G., Rozo E., 2013, *Physics reports*, 530, 87
- Wilson M. J., Peacock J. A., Taylor A. N., de la Torre S., 2017, *Monthly Notices of the Royal Astronomical Society*, 464, 3121
- Xavier H. S., Abdalla F. B., Joachimi B., 2016, *Monthly Notices of the Royal Astronomical Society*, 459, 3693
- Zhou R., et al., 2021, *Monthly Notices of the Royal Astronomical Society*, 501, 3309
- Zhou R., et al., 2022, arXiv preprint arXiv:2208.08515
- Zou H., et al., 2017, *Publications of the Astronomical Society of the Pacific*, 129, 064101
- de Putter R., Gleyzes J., Doré O., 2017, *Physical Review D*, 95, 123507

This paper has been typeset from a \LaTeX file prepared by the author.